Hidden Structural States of Proteins Revealed by Conformer Selection with AlphaFold-NMR

Yuanpeng J. Huang[1]*, Theresa A. Ramelot[1], Laura E. Spaman[1], Naohiro Kobayashi[2], and Gaetano T. Montelione[1]*

[1]Department of Chemistry and Chemical Biology, Center for Biotechnology and Interdisciplinary Sciences, Rensselaer Polytechnic Institute, Troy, New York, 12180 USA
[2]NMR Science and Development Division. RSC, RIKEN, 1-7-22 Suehiro-cho, Tsurumi-ku, Yokohama City, Kanagawa 230-0045, JAPAN

Abstract

We introduce AlphaFold-NMR, a novel approach to NMR structure determination that reveals previously undetected protein conformational states. Unlike conventional NMR methods that rely on NOE-derived spatial restraints, AlphaFold-NMR combines AI-driven conformational sampling with Bayesian scoring of realistic protein models against NOESY and chemical shift data. This method uncovers alternative conformational states of the enzyme *Gaussia* luciferase, involving large-scale changes in the lid, binding pockets, and other surface cavities. It also identifies similar yet distinct conformational states of the human tumor suppressor Cyclin-Dependent Kinase 2-Associated Protein 1. These studies demonstrate the potential of AI-based modeling with enhanced sampling to generate diverse structural models followed by conformer selection and validation with experimental data as an alternative to traditional restraint-satisfaction protocols for protein NMR structure determination. The AlphaFold-NMR framework enables discovery of conformational heterogeneity and cryptic pockets that conventional NMR analysis methods do not distinguish, providing new insights into protein structure-function relationships.

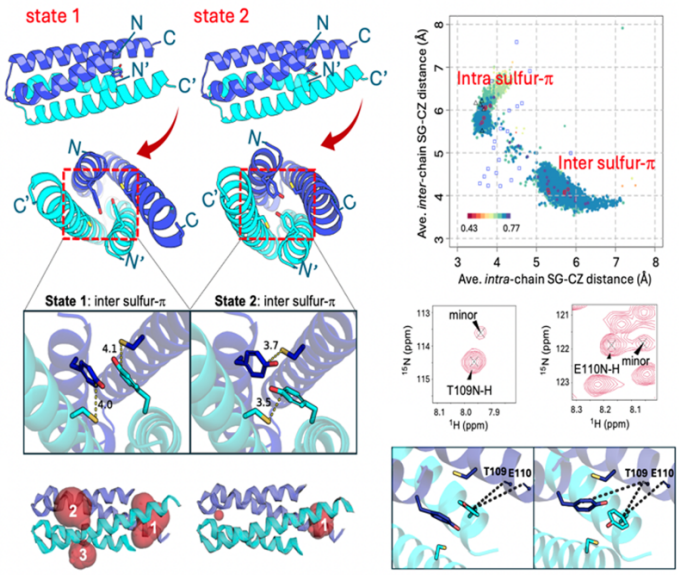

*Corresponding authors. Email: huangy26@rpi.edu, monteg3@rpi.edu

Yuanpeng J. Huang orcid: 0000-0002-3374-786X email: huangy26@rpi.edu
Theresa A. Ramelot orcid: 0000-0002-0335-1573 email: ramelt2@rpi.edu
Laura E. Spaman orcid: 0000-0003-3451-9620 email: spamal@rpi.edu
Naohiro Kobayashi orcid: 0000-0001-5136-2077 email: naohiro.kobayashi@riken.jp
Gaetano T. Montelione orcid: 0000-0002-9440-3059 email: monteg3@rpi.edu

Key words: Solution NMR, AlphaFold2, *Gaussia* luciferase, Bayesian scoring function, conformer selection, conformational dynamics, enhanced sampling.

Abbreviations: AF2 – AlphaFold2 multimer; AFsample – AlphaFold2 with enhanced sampling; AI – Artificial Intelligence; CCC – Lin's Concordance Correlation Coefficient, CDK2AP1 – Cyclin-Dependent Kinase 2-Associated Protein 1, CI – statistical Confidence Interval; LDDT – Local Difference Distance Test score, a superimposition independent metric of structural similarity; NOE – Nuclear Overhauser Effect; GLuc – *Gaussia* luciferase; NOESY – NOE SpectroscopY; pLDDT – predicted per-residue LDDT from AF2; <pLDDT> - pLDDT score averaged over all residues in the protein sequence; $pLDDT_{avg}$ – average per-residue pLDDT across a set of models; PSVS – Protein Structure Validation Software suite; pTM – predicted TM score for overall protein structure from AF2; RCI – Random Coil Index for assessing conformational flexibility from chemical shift data; $RCI_{0.6}$ – Random Coil Index scaled by 1/0.6; RDC – Residual Dipolar Coupling; RMSD – Root Mean Squared Deviation; RMSF - Root-Mean-Squared Fluctuation of atomic positions; $RMSF_{ENS}$ – RMSF for an ensemble of conformers; $RMSF_{RCI}$ – Random Coil Index scaled for RMSF comparison; RPF-DP score – Recall, Precision, F-measure, and Discrimination Power score; SA – surface area; SCC – Spearman's correlation coefficient; SEM – standard error of the mean; TM score – template model score, a measure of structural similarity.

Introduction

Recent advances in molecular modeling using artificial intelligence (AI), such as AlphaFold2 (AF2), have revolutionized protein structure determination. For example, AF2 has demonstrated high accuracy in modeling relatively rigid protein structures[1]. AF2 models are now widely used as phasing models in X-ray crystallography[2,3] and to guide structural analysis in cryogenic electron microscopy (cryoEM), small angle X-ray scattering (SAXS), and NMR [for examples see refs [4-8]]. While AF2 was not designed for studying protein dynamics, it has been adapted to predict flexible regions[1,9-13], alternative conformations[14-22], and populations of conformational states[23-25] of proteins. However, the general problem of identifying biologically relevant structures from these computational ensembles remains challenging, particularly for dynamic proteins.

To address this challenge, we developed AlphaFold-NMR (AF-NMR), which combines AI-driven enhanced sampling with NMR-guided conformational selection. First, an enhanced sampling AF2 protocol is used to generate a wide range of physically-reasonable structural models. The generated models are clustered, scored against NMR data, and validated using NOESY Double Recall analysis. Compared to conventional NMR restraint-based modeling, AF-NMR overcomes inaccuracies that result from interpreting NOESY data as distance restraints[26,27], particularly those arising from conformational averaging, and enables accurate determination of both single and multi-state protein structures. While AFsample[21], a neural network dropout method, is used here for enhanced sampling; other comprehensive sampling strategies could also be incorporated into our protocol. This approach provides a robust framework for studying dynamic proteins and uncovering otherwise hidden conformational states of proteins.

We selected *Gaussia* luciferase (GLuc) for NMR-guided conformational selection due to its dynamic nature and likelihood of sampling multiple states in equilibrium[28,29]. GLuc, an 18.2 kDa monomeric enzyme from *Gaussia princeps*, catalyzes the oxidation of coelenterazine, producing a bright blue bioluminescent signal[30]. Previous NMR studies have highlighted its extensive conformational flexibility (PDB_ID: 7d2o[28,31]; PDB_ID: 9lfa[32]), and it was classified as a challenging target in CASP14 (target T1027) due to the absence of homologous structure templates for comparative modeling[29]. Notably, there are significant structural differences between the computed AF2 model and the experimental NMR structure, particularly in the positions of three helices[29]. This discrepancy is of interest because AF2 models of small, relatively rigid proteins often rival the accuracy of experimental NMR structures[4,6,7,29,33,34], despite NMR structures being excluded from AF2 training[1]. However, for highly-flexible proteins like GLuc, these differences highlight AF2's limitations in capturing the solution-dominant states[11,29,35-38]. Both GLuc models are supported by distinct subsets of NOEs, leading us to reason that NOESY data could be used for conformational selection. These characteristics make GLuc an excellent system for exploring NMR-guided AI-enhanced sampling methods for modeling multiple conformational states of proteins.

Using AF-NMR, we uncovered multiple conformational states of GLuc that collectively fit NOESY and chemical shift data better than the original restraint-generated NMR structure. A single set of chemical shifts indicates that these conformations are in fast -exchange on the NMR timescale. In one state, a loop between helices H5 and H6 adopts a closed conformation, forming a lid over a cryptic pocket proposed to be the enzyme's active site[31,32]. In a second data-supported state, the lid is open, exposing the pocket, while subtle helical rearrangements further expand the pocket. A second surface pocket containing additional functionally-important residues is also observed. Comparing the AF-derived open and closed

states to the NOESY data reveals distinct subsets of NOEs unique to each conformation, validating these two previously unrecognized structural states.

As a second example of AF-NMR revealing hidden structural states, we examined the human tumor suppressor Cyclin-Dependent Kinase 2-Associated Protein 1 (CDK2AP1). CDK2AP1, encoded by the *doc-1* (deleted in oral cancer 1) gene, is a specific inhibitor of CDK2[39]. Its loss or downregulation is associated with increased metastasis in various cancers, including liver and breast cancer [40-42]. CDK2AP1 is a highly conserved protein that functions as both a cell cycle and epigenetic regulator[43]. It has multiple binding partners and forms a subunit of the nucleosome remodeling and histone deacetylation (NuRD) complex[44-46], which regulates embryonic stem cell differentiation. The previously determined NMR structure of CDK2AP1 revealed a homodimeric four-helix bundle (residues 61-115) with intrinsically disordered 60-residue N-terminal regions[47]. Unlike GLuc, which exhibits large-scale structural heterogeneity, the flexibility of the $CDK2AP1_{61-115}$ four-helical bundle is largely confined to its C-terminal helices, as indicated by ^{15}N relaxation experiments[47]. Although Cys105 is considered essential for function and has been proposed to form an interchain disulfide bond[48], the solution NMR structure indicates that these sulfur atoms are too far apart (4.4 - 10.2 Å) to form a covalent bond[47]. Using AF-NMR, we identified two conformational states of $CDK2AP1_{61-115}$ in dynamic equilibrium, distinguished by interchain and intrachain Cys S– aromatic π interactions. These alternative structural states suggest a previously unrecognized role for Cys105: dynamically switching between interchain and intrachain sulfur–π interactions with Tyr63, and reveal previously hidden cryptic pockets on the surface of the CDK2AP1. These examples highlight the utility of AF-NMR for uncovering conformational states that fit to experimental data by *conformer selection*, offering a powerful alternative to conventional restraint-based protocols for protein NMR structure determination.

Results

Comparison of conventional NMR and standard AF2 models of GLuc using NOESY Double Recall. Discrepancies between AF2 models and experimental NMR structures for GLuc, as well as the identification of distinct NOEs supporting each model[29], motivated its selection for this study. **Figure 1a** compares the conventional NMR structure (PDB ID 7d2o[28]) and models generated using AF2 Colabfold (see Methods). NOESY Double Recall analysis (**Figure 1b**) highlights regions of structural differences supported by NOESY peak data, with 543 distinct NOEs for the NMR model (blue dots) and 138 distinct NOEs for the AF2 models (orange dots). Key structural differences include the packing of N-terminal helix H1 inside the core (in NMR_{7d2o}) versus helices H10/H11 packing against the core (in the standard AF2 model).

A more recent solution NMR structure of GLuc, PDB ID 9fla[32], exhibits similar core architecture (**Supplementary Figure S1**). Both NMR_{7d2o} and AF2 structures share five disulfide bonds and a scaffold of seven helices, defined as "core helices", although some significant modeling differences are reported. For comparisons, the NMR_{7d2o} structure was chosen over NMR_{9fla}, as it has more complete and accessible NOESY and chemical shift data.

Comparison of conventional NMR and standard AF2 models of GLuc using flexibility metrics. Experimental flexibility metrics, including the random coil backbone chemical shift index (RCI) and ^{15}N-^{1}H heteronuclear NOE (hetNOE), were compared with AF2 pLDDT scores, a measure of local model uncertainty (**Figure 1c,d**). While pLDDT scores generally correlate with regions of conformational

flexibility[1,9-13,49], this correlation is appreciated to be imperfect and fails to capture gradations in dynamics within highly flexible regions[13]. For GLuc, RCI and hetNOE profiles are strongly correlated (Spearman correlation coefficient, SCC: -0.75), while RCI and per-residue pLDDT values show weaker correlations (SCC: -0.56; **Figure 1c**).

The pLDDT vs RCI comparison plot (see Methods) illustrates structural regions of concordance and discrepancy, with good agreement in the rigid core (helices H3–H5 and H6–H9), where high pLDDT scores, low RCI values, and high hetNOE values are observed (**Figure 1c,d**). In contrast, flexible regions, such as the H5/H6 loop, have high RCI and low hetNOE values but relatively high pLDDT scores, suggesting an underrepresentation of flexibility in the AF2 models. Similarly, helix H1 has low RCI and high hetNOE values (indicating low flexibility) but exhibits low pLDDT scores in standard AF2 models. These discrepancies correspond to regions of significant structural differences between AF2 and NMR models (**Figure 1a**), suggesting the presence of multiple conformational states.

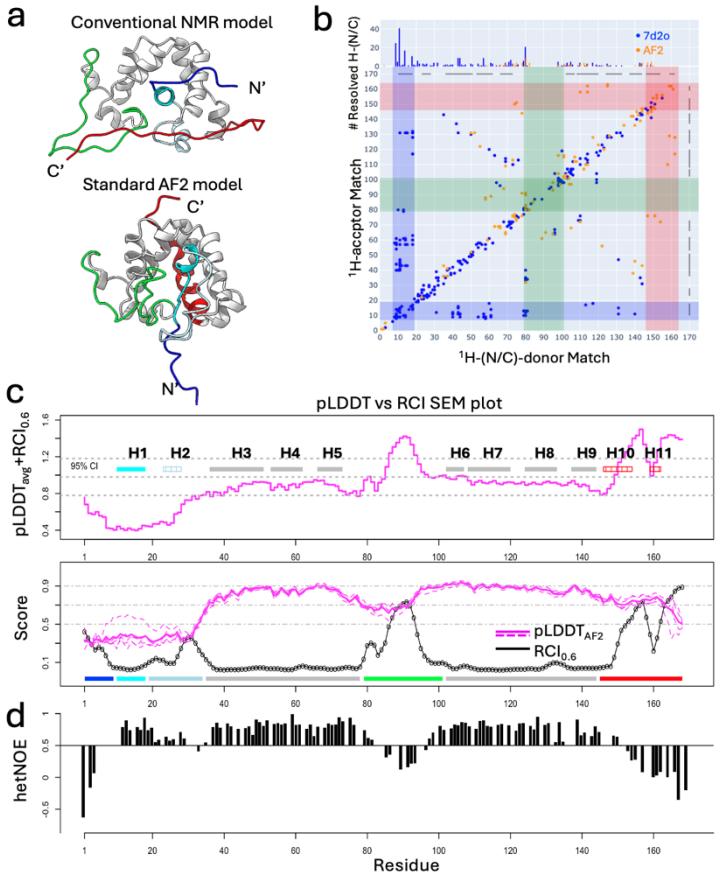

Fig 1. Comparison of conventional NMR and AF2 models of GLuc. (a) Ribbon diagrams of the NMR_{7d2o} structure (top) and standard AF2 model (bottom) with the structurally variable regions colored and conserved regions in gray. Color scheme: blue (N-terminal disordered region, residues 1-9), cyan (helix H1, residues 10-18), light blue (helix H2 and loop, residues 19-34), green (loop between H5 and H6, residues 79-101), red (C-terminal disordered region, residues 146-168), and gray (core α-helices H3 - H9). In the AF2 models, the C-terminal region (red) forms a kinked "broken helix" (residues 146-154 and 159-162). **(b)** Double Recall plot (see Methods) comparing NMR and AF2 models. Contact maps show inter-residue NOEs unique to the NMR model (blue), AF2 model (orange), or overlapped (brown). Blue and red stripes highlight contacts between the N-terminal helix H1 (residues 7-19) or C-terminal helices H10/H11 (residues 146-164) and core residues. **(c)** Comparison of pLDDT and RCI data. (Top) Comparison SEM plot (see Methods) between $pLDDT_{avg}$ and $RCI_{0.6}$ with helices labeled. The most flexible helices (H2, H10, and H11) are marked with stripes. The average and 95% confidence intervals (**Eqn. 3**) are shown as gray dashed lines. (Bottom) Per-residue pLDDT (dashed line for each model and solid line for average) and $RCI_{0.6}$ scores. The residue segment color scheme of **Fig. 1a** is shown along the bottom. **(d)** Previously published per-residue backbone heteronuclear ^{15}N-^{1}H hetNOEs monitoring backbone dynamics[28].

AI-based modeling with enhanced sampling generates conformational diversity of GLuc. We tested whether AI-based modeling with enhanced sampling could produce alternative models that better fit the NMR NOESY and RCI data compared to standard AF2 models. This approach, summarized in **Supplementary Figure S2**, uses the AFsample method[21,50], which generates diverse models by varying parameter settings. Since GLuc has a relatively shallow MSA (229 sequences), MSA-based methods such

as AF_alt[14] and AF_cluster[20] failed to generate models with high NOESY recall scores and were not considered further. The resulting AFsample models were evaluated by TM score and NOESY recall scores (**Figure 2a**), which quantify the fraction of NOESY peaks explained by short interatomic distances. While most AFsample models had lower NOESY recall scores, some achieved scores as high as 0.88, surpassing the standard AF2 model (0.86) and approaching the conventional NMR models (0.89) that have been forced to fit as many NOESY-based restraints as possible.

Principal component analysis (PCA) grouped AFsample models into four clusters (α, β, γ, and δ; **Figure 2b**). These models were scored against NOESY and RCI data using Bayesian posterior P(model | NMR data) metrics (Methods**; Supplementary Fig. S3**). Clusters α (~20%) and β (~20%), with high NOESY recall scores, represented plausible conformations, while clusters γ (~25%) and δ (~35%) with lower recall scores were less likely. Structural differences among clusters were primarily driven by the orientation of helix H1 (PC1) and the position of the H5/H6 loop (PC2; **Supplementary Figure S4**).

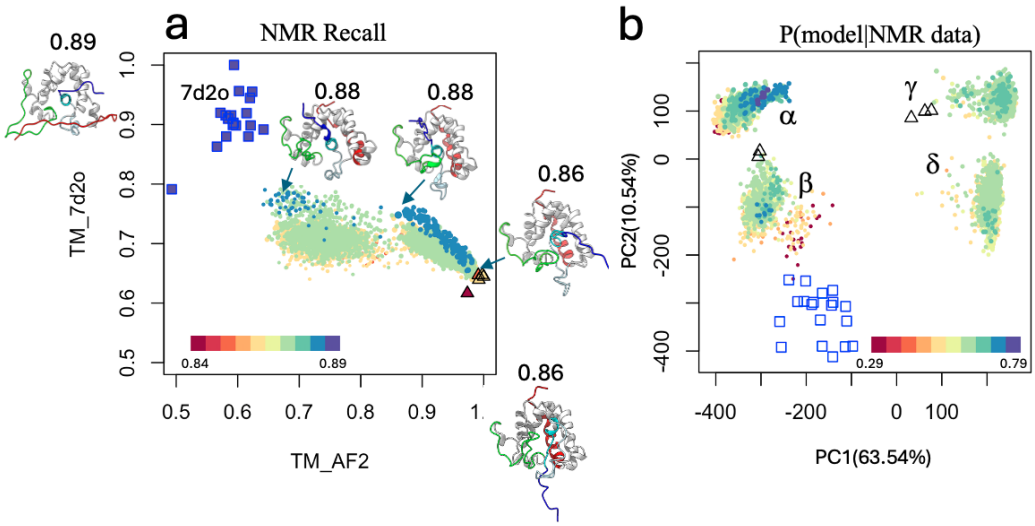

Fig 2. Diversity of AFsample models. (**a**) TM plots of AFsample vs NMR_{7d2o} and AF2 models. TM_AF2 scores are calculated by comparing each conformer with the standard AF2 rank1 model (for ordered regions 42-78 and 93-162). TM_NMR_{7d2o} scores are calculated by comparing each conformer with the medoid NMR_{7d2o} model (model #3, for ordered regions 7-19, 34-81, and 95-143). The dot plot for each conformer is colored by its NOESY recall score for AFsample (circles), conventional NMR_{7d2o} (squares), and standard AF2 (triangles) models. (**b**) 2D projections of $C\alpha$ coordinate principal component analysis (PCA). Models are colored by Bayesian posterior score P(model|NMR data), defined in Methods. Conventional NMR_{7d2o} models are indicated as blue open squares and standard AF2 models are indicated as black open triangles. In all panels, the size of each AFsample point is scaled by the pTM score of the model, the bigger the point the higher the pTM. The four PCA clusters (α, β, γ, and δ) are labeled in panel **b**.

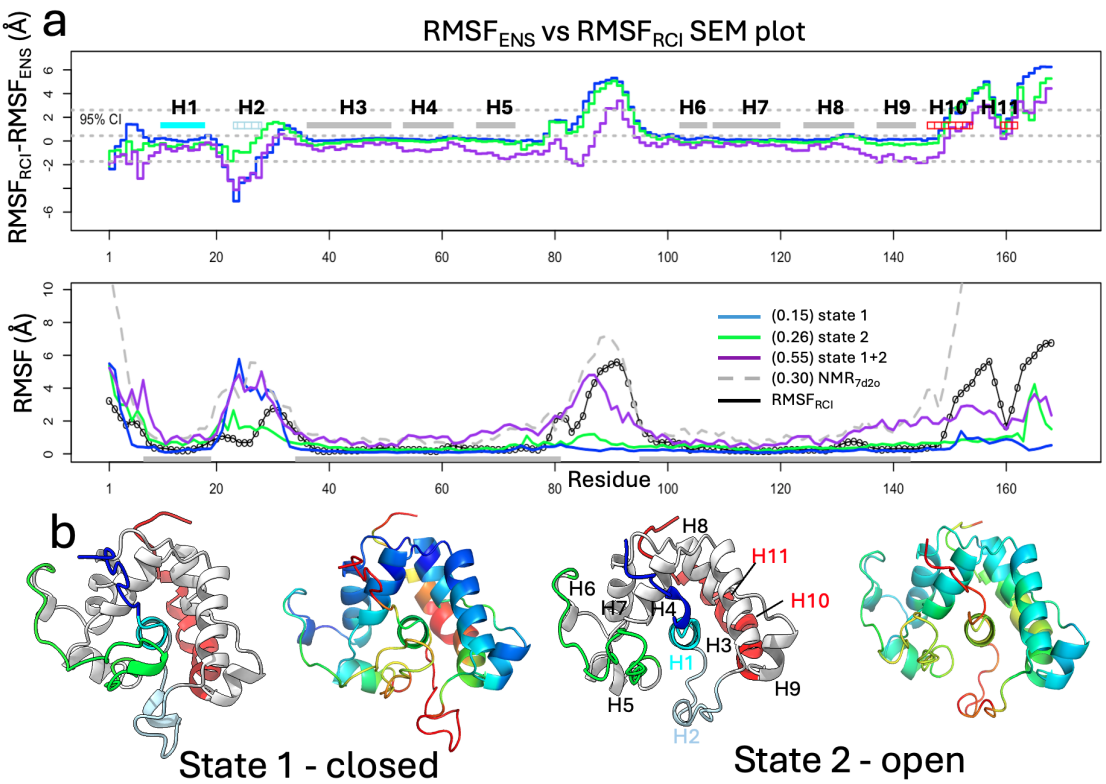

Fig. 3. Combining states by matching RCI data with modeled atomic RMSFs. **(a)** (top) Comparison SEM plots of $RMSF_{RCI}$ - $RMSF_{ENS}$ for state 1, state 2, and their 1:1 mixture. (bottom) $RMSF_{ENS}$ for state 1, state 2, their mixture, and for NMR_{7d2o} compared with $RMSF_{RCI}$, with "well defined" NMR_{7d2o} regions shown as gray bars at the bottom and used in structural alignments for $RMSF_{ENS}$ calculations. CCC scores for $RMSF_{ENS}$ of selected conformers vs $RMSF_{RCI}$ are provided in parenthesis in panel (a) inset. (**b**) Conformer-selected AlphaFold-NMR multi-state structures of GLuc. (left pair) State 1 (rank 3 model) is colored by structural elements and by per-residue pLDDT scores, respectively. (right pair) State 2 (rank1 model) colored the same.

Conformer selection and identification of states. Conformational states identified by PCA were scored using experimental NMR data to calculate Bayesian posterior probability P(model | NMR data) (**Eqn. 11)** metrics, enabling the selection of models from each cluster that best fit the data (Methods). Four candidate single-state ensembles (α5, β5, γ5, and δ5) were created from the top five highest-scoring models of each cluster, ranked by their average P(model | NMR data) scores. The ensemble α5, which had the highest P(model | NMR data), was identified as state 1.

Residue-by-residue comparisons of ensemble-based backbone Cα RMSF values ($RMSF_{ENS}$) calculated from state 1 with experimental RMSF estimates from chemical shift-based RCI data ($RMSF_{RCI}$) revealed discrepancies, interpreted as limitations of single-state modeling (blue line in **Figure 3a**). To improve this agreement, state 1 was combined with each of the other candidate single-state ensembles β5, γ5, and δ5, to create composite $RMSF_{ENS}$ predictions, assuming fast (or fast-intermediate) exchange. Agreement with the experimental $RMSF_{RCI}$ profile was quantified using Concordance Correlation Coefficients (CCCs) (**Eqn. 12**). For GLuc, the combination of state 1 and the ensemble β5 maximized the CCC (0.55), outperforming the other two-state combinations (0.12 and 0.06; **Supplementary Figure S5**). This combined CCC is also significantly higher than that of the original NMR_{7d2o} structure (0.30), or the standard AF2 model (0.05). Accordingly, clusters γ and δ, with flipped helix H1 orientations, were

excluded due to low composite CCC values. This flipped H1 orientation was also not supported by NOESY data. The ensemble β5 was therefore identified as state 2.

Comparison plots of $RMSF_{ENS}$ vs $RMSF_{RCI}$ (**Figure 3a**), show improved agreement for the mixture of states 1 and 2 compared to either of the two single states, particularly in regions of the H5/H6 loop, and the C-terminal helix H10/H11. Representative structures of the "closed" (state 1) and "open" (state 2) conformations are shown in **Figure 3b**. In particular, the $RMSF_{ENS}$ fluctuations for the H5/H6 loop ("lid") align more closely with the $RMSF_{RCI}$ data for the combined state 1 and 2 models than for individual states.

The AF-NMR ensemble, consisting of ten models from combined states 1 and 2, was further assessed by comparing per-residue pLDDT values with NMR RCI data (**Supplementary Figure S6**). Each state exhibited distinct pLDDT profiles, with per-residue average pLDDT ($pLDDT_{avg}$) values for states 1 and 2 showing improved correlation with experimental RCI data compared to standard single-state AF2 models (improved SCCs, **Supplementary Figure S6**), especially for helix H1. Most residues agree within the 95% confidence interval except the H5/H6 loop, which requires a combined model for accurate representation. Using $pLDDT_{avg}$ values as proxies for *state-specific conformational flexibility*, helices H3–H5 and H6–H9 have low flexibility in both states. Helix H2 and the H5/H6 loop are more flexible in both states, while helix H1 exhibits greater flexibility in state 2, and the C-terminal helices H10 and H11 are more flexible in state 1.

Cross-validation of conformational states by NOESY Double Recall analysis. NOESY Double Recall analysis confirmed that the combination of states 1 and 2 better explains the NMR NOESY data than single-state models, including NMR_{7d2o} (**Figure 4a; Supplementary Figure S7 and Table S1**). State 1 uniquely explains 185 NOEs (101 long-range) compared to NMR_{7d2o}, while state 2 uniquely explains 164 NOEs (71 long-range). The combined ensemble of states 1 and 2 accounts for 218 NOESY peaks (116 long-range) that are not consistent with the NMR_{7d2o} structure, confirming that this two-state ensemble fits the NOESY data more effectively than the NMR_{7d2o} model. However, a small number of NOESY peaks are not explained even by the combined ensemble, suggesting additional states may exist in dynamic equilibrium (**Supplementary Table S1**). Additionally, Double Recall analysis was used to identify distinct subsets of NOEs for each state (**Figure 4a-d**) that demonstrate the ability of AF-NMR to resolve multiple conformational states and capture dynamic transitions essential for GLuc's function.

Conformational ensembles and structural quality assessment. The conformational ensembles for states 1 and 2 have been deposited in the Protein Data Bank (PDB ID: 9A8V). These ensembles exhibit significantly better structure quality metrics compared to conventional NMR structures 7d2o and 9fla (**Supplementary Tables S2–S5**). NOESY RPF scores, which compare global NOESY peak list data with structural models, are similar for state 1, state 2, and NMR_{7d2o} (**Supplementary Table S6**); NOESY data for 9fla are unavailable.

Structural features of GLuc states 1 and 2. States 1 and 2 represent two substantially-populated alternative conformations of GLuc in fast-exchange (or fast-intermediate-exchange) dynamic equilibrium. A detailed structure-function analysis (**Figure 4b-f**) reveals that the major difference between these states lies in the conformation of the H5/H6 thumb-shaped loop. In the "closed" state 1, the loop forms a "lid" capping a surface binding pocket (**Figure 4c,e**), supported by ~8 NOEs (residues 88–91 and 10–16; **Figure 4a**). In the "open" state 2, the loop moves away, exposing a cryptic pocket and allowing helix H5 to interact with helix H7 (~15 NOEs; **Figure 4d,f**). Small changes in interhelical angles (H3–H4 and H7–

H8) accompany this transition, with state 1 forming a compact "pincher" structure and state 2, having an expanded pocket. Helix H2 transitions from an α-helix in state 1 to a 3_{10} helix in state 2. Both state 1 and state 2 include a C-terminal "broken helix", defined by two helices H10/H11. This broken helix is packed closer to the helices H1 and H7 in state 1 than in state 2. Specifically, in state 1 helices H10/11 have ~12 NOEs interacting with helix H7 (including 5 NOEs to Met110) and the end of helix H1 (**Figure 4a,b**). Residue Met110 exhibits several NOEs unique to state 1 (**Figure 4a**) indicating its potential role in modulating the two-state equilibrium.

The transition between states also reshapes two surface pockets of GLuc (**Figure 4e,f**). In state 1, pocket #1 is small and variable (~30 – 110 Å^3), while in state 2 pocket #1 expands (~ 170Å^3) and a new larger cryptic pocket #2 appears (~600–800 Å^3). Residues Arg76 (in pocket #1) and Arg147 (in pocket #2) both have critical roles in GLuc bioluminescence[32,51], and these structural changes likely impact substrate binding and enzymatic function (see Discussion).

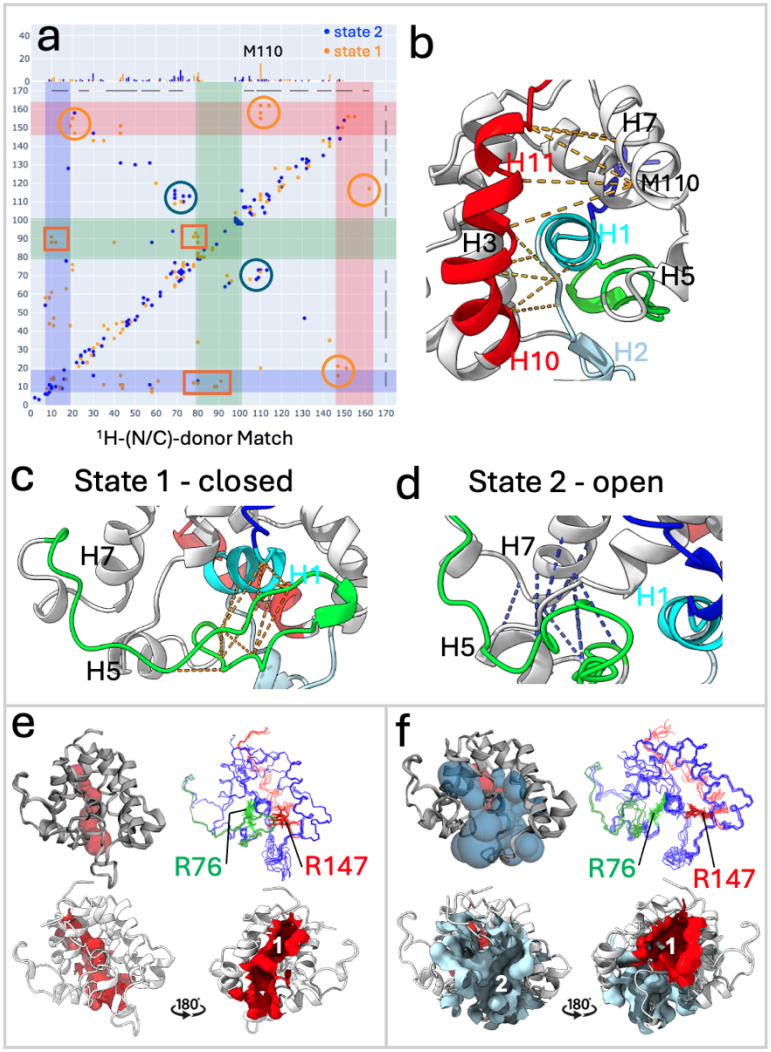

Fig. 4. Detailed analysis of conformer-selected AlphaFold-NMR multi-state structures of GLuc. (**a**) Double Recall plot of AF-NMR state 1 vs state 2, illustrating key inter-residue contacts distinguishing these states; orange dots support "closed" state 1, blue dots support "open" state 2, and brown dots are overlapped blue and orange dots. Scaling of the top inset is the same as for **Figure 1b**. (**b**) "Closed" state 1 with key NOEs indicated as orange dashed lines (corresponding to orange dots in the red shaded region of panel **a**) includes transient helices H10 and H11 (red) which contribute to forming part of pocket #1. (**c**) "Closed" state 1 with key NOEs indicated as orange dashed lines (corresponding to orange dots in the green shaded region of panel **a**). (**d**) "Open" state 2 with key NOEs indicated as blue dashed lines (corresponding to blue dots in the blue circles of panel **a**). In panels **b**, **c**, and **d**, the dashed lines connect the Cα-Cα atoms of the corresponding residues. **(e)** "Closed" state 1 includes a pocket (pocket #1, red), while **(f)** "open" state 2 has both a larger pocket #1 and a new pocket (pocket #2, blue). In the "closed" state 1, the H5/H6 loop contacts helix H1 closing binding pocket #2, while in the "open" state 2, this loop moves close to helices H5 and H7, opening binding pocket #2. The pocket of "closed" state 1 (red pocket #1, shown for state 1, rank 3 model with highest pTM score in cluster α) has a pocket volume of 106 Å^3, while "open" state 2 includes not only a wider red pocket #1 (shown for state 2, rank 1 model with the highest pTM score in cluster β, with volume 173Å^3), but also a new large cryptic blue pocket #2, volume 786 Å^3. Side chains of functionally-important residues Arg76 (green) in pocket #1 and Arg147 (red) in pocket #2 are shown in state 1 and state 2, respectively (panels **e,f** – upper right).

Conformational switching of CDK2AP1. As a second example, the AF-NMR method was also applied to investigate the dynamic structure of CDK2AP1, a homodimeric right-handed four-helical bundle[47]. Conventional NMR and standard AF2 models of CDK2AP1(residues 61–115) are similar (RMSD: 0.99–1.21 Å) but neither position Cys105 sulfur atoms within 3 Å for disulfide bond formation, which has been suggested (but not demonstrated) to be important for CDK2 binding[48]. Using AF-NMR conformational selection (**Supplementary Figure S2**), 6000 AFsample models were analyzed and grouped into four clusters (α, β, γ, and δ; **Figure 5a**). Most models belong to clusters α (~50%) and β (~47%), while clusters γ (~2%) and δ (~1%) represent alternative packing arrangements (**Supplementary Figure S8**) that are excluded under the conditions of the NMR study by NOESY data.

The AFsample models were scored against experimental NMR data to estimate P(model | NMR data) (**Figure 5a,b; Supplementary Figure S9**). The five top-scoring conformers from clusters α and β were identified as states 1 and 2, respectively. Comparison of $RMSF_{ENS}$ vs $RMSF_{RCI}$ data shows improved agreement when states 1 and 2 are combined (CCC = 0.70), outperforming single-state models (CCC = 0.39 for state 1; CCC = 0.14 for state 2; **Supplementary Figure S10**). This plot also reveals greater flexibility in the C-terminal region of helices H2/H2' in state 1 compared to state 2, which is also reflected in the lower state-specific pLDDT scores (**Supplementary Figure S11**). The two-state model for CDK2AP1 was further validated by NOESY Double-Recall analysis, which identified peaks specific to each state (**Supplementary Figure S12 and Table S7**). However, as the structures of these two states are very similar (**Figure 5c,d**; pairwise backbone RMSDs: 0.56 - 1.32 Å) and the spectra of these homodimeric conformers are highly degenerate, only a few NOESY peaks are unique to one or the other conformational states. Of the observed NOEs, 22 (16 long-range) were unique to state 1, while 23 (3 long-range) were unique to state 2. While most chemical shifts do not distinguish the two states, peak doubling of Thr109 and Glu110 HNs, which experience ring-current shifts, indicates slow exchange between these major (~85%) and minor (~15%) states (**Figure 5e,f,g; Supplementary Figure S13**).

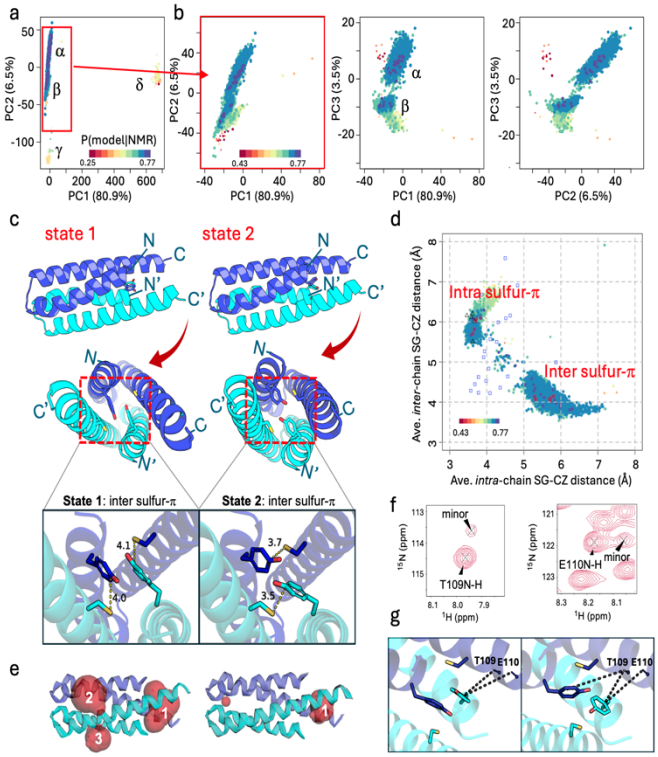

Fig 5. Hidden conformational states of CDK2AP1. (a) PCA based on the Cα-Cα distance matrix, showing structural variation along PC1 and PC2. Clusters (α, β, γ, and δ) correspond to distinct conformational states. **(b)** Expanded PCA plots for clusters α and β (red rectangle in (a)). Clusters α and β are well separated by PC3. Model PCA coordinates are colored based on values of P(model | NMR data), defined in the inset of panels a,b. The size of each point is coded by the pTM score of the model, the larger the point the higher the pTM. **(c)** Ribbon diagrams illustrating inter S-π state (state 1, rank 2) with key Sγ-Cζ inter chain distances (4.0 and 4.1 Å^2) and intra sulfur-π state (state 2, rank 1) with Sγ-Cζ intra-chain distances (3.5 and 3.7 Å^2). Side chains of Tyr63 and Cys105 are displayed in stick representation with corresponding distances labeled. **(d)** Scatter plot of average intra-chain and inter-chain distances of Tyr63-Cζ to Cys105-Sγ for all models from clusters α and β. The top 5 models from clusters α and β are circled in red. Conventional NMR models (PDB_ID 2kw6) are indicated as blue open squares and standard AF2 models are indicated as black open triangles. **(e)** Surface pockets identified by CASTpFold[52] (**Supplementary Figure S14**). The state 1 model with the largest pockets (#1-#3) is shown.

The state 2 model has a smaller pocket #1, while pockets #2 and #3 were each < 2 Å^3. These surface cavities are shown in translucent red. **(f)** ^{15}N SOFAST HMQC spectral regions showing peaks of T109 and E110 HN corresponding to major and minor states. **(g)** NHs of T109 and E110 are shown as sticks with close distances (< 7.5 Å) to Tyr63 rings indicated with dashed lines.

None of the cluster α and β conformers have Cys105 sulfur atoms with distances suitable for disulfide-bond formation (< 3 Å); however, favorable geometries for sulfur – aromatic π interactions between Cys105 and Tyr63 were observed. These interactions, along with differences in surface pockets, distinguish states 1 and 2 (**Figure 5c-e**). In state 1, *inter*-chain sulfur – π interactions and Tyr63 π-π stacking lead to a more open structure between the N- and C-terminal ends of the four helices, forming an 'end' cavity (pocket #1). Several residues in this pocket exhibit peak doubling due to slow conformational exchange (**Figure 5e, Supplementary Figures S13 and S14**). Pockets #2 and #3 contain multiple basic residues (Lys and Arg). In contrast, state 2 features *intra*-chain sulfur - π interactions, leading to a more compact structure with a smaller pocket #1**,** while pockets #2 and #3 are significantly reduced or absent (**Figure 5c and e, right, Supplementary Figure S14**). Upfield shifts in the Cys105 Hβ protons support both intra- and inter-chain sulfur–π interactions due to ring-current effects (Ringer, 2007). The conventional NMR structure (2kw6) captures elements of both states, but does not fully represent either due to conformational pinning[53]; its intra- vs inter-chain Cys105 Sγ - Tyr63 Cζ distances fall between the two states (**Figure 5d**). Standard AF2 consistently generates only state 2, favoring the more compact structure.

Discussion

Conformational selection with AF-NMR. The AF-NMR method combines AlphaFold modeling with enhanced sampling and NMR-guided conformational selection, offering a novel approach to protein structure determination. By generating diverse conformers and scoring them against NMR data, including NOESY recall and RCI metrics, AF-NMR identifies single or multiple conformational states that best fit the experimental data. Alternative states are further validated using NOESY Double Recall analysis. Unlike conventional restraint-based NMR modeling, which relies on distance constraints to build a single-state model, AF-NMR applies a Bayesian framework to integrate sample-specific NMR data with AF2 pTM and per-residue model reliability scores (pLDDTs) allowing for selection of one or more conformational states that together best fit the NMR data.

Conventional restraint-based NMR approaches can result in inaccurate models, particularly when dealing with conformationally heterogeneous systems. Sparse NMR data from transiently populated states may be insufficient for accurate modeling, while conflicting NOEs arising from multiple states can result in partially satisfied restraints or overly constrained structures. These issues can lead to conformational "pinning," where the requirement to simultaneously satisfy distance restraints arising from distinct states forces the model into an unrealistic compromise[53,54]. Difficulties also arise from peak degeneracy and assignment of ambiguous NOEs in flexible regions. In contrast, AF-NMR allows for the explicit selection and combination of multiple conformational states without distortions from restraints, leveraging AI-based modeling to generate candidate structures that align with the experimental data.

Consistent with other studies[1,9-13,49], we observe that AF2 residue-specific pLDDT scores reliably distinguish ordered from disordered regions. However, discrepancies arise in regions where pLDDT does

not correlate with experimental flexibility metrics, such as RCI and hetNOE. Here we compare RCI with pLDDT of standard AF2 models, an estimate of the local rigidity (or certainty). We reasoned that discordance between these metrics can be an indication of conformational diversity not captured by the standard AF2 models. Using enhanced sampling protocols, such as AFsample, AF-NMR generates more diverse conformers and improves the nonlinear agreement between pLDDT and RCI (i.e., |SCC(pLDDT, RCI)|). In cases where single-state models fail to fully explain the experimental data, combining multiple state models enhances agreement, providing a more accurate representation of dynamic structural ensembles.

Conformational state bias in AlphaFold modeling has been increasingly recognized, with several studies showing how memorization of states in training data can bias predictions of proteins with alternative native structures[35,37,38]. If experimental structures which capture only one (or some) of the states were included in its training set, conformational state bias may prevent AF from finding alternative states. While AF2 was not trained on NMR structures[1], state bias may still occur if X-ray or cryoEM homolog structures of the target protein were included in its training set. In this study, we avoided such bias by selecting proteins with no homologous structures in the training set. However, where bias is suspected, alternative sampling strategies, such as varying MSA inputs or even retraining AlphaFold with specific exclusions may be necessary to ensure unbiased sampling.

Although not yet broadly adopted by the structural biology community, we and others have emphasized the potential value of Bayesian formalisms in NMR data analysis, particularly for integrative modeling (Andrec *et al*., 1999; Andrec *et al*., 2000; Hoch and Stern, 2005; Rieping *et al*., 2005; Nilges *et al*., 2008; Rieping *et al*., 2008). The Bayesian framework used in AF-NMR can support incorporation of diverse NMR data types, including residual dipolar coupling, back-calculated chemical shift, chemical exchange, nuclear relaxation, paramagnetic relaxation enhancements, and pseudocontact shift data, offering a comprehensive toolset for conformer selection and validation. As an evolving method, AF-NMR may also benefit from integrating alternative AI-based modeling methods such as AlphaFold3[55], RosettaFold[56], or others[57,58]. Incorporating alternative AI-based enhanced sampling techniques[17] will also further expand AF-NMR's ability to capture conformational heterogeneity and dynamics.

Dynamic Structural Features of GLuc. AF-NMR reveals distinct conformational states of GLuc that are consistent with previous structure-function studies[28,31,32,51] but provide additional insights into its structural transitions. The H5/H6 loop ("lid") undergoes a dynamic shift between a "closed" state 1, where it caps pocket #2, and an "open" state 2, where the cryptic pocket #2 is exposed. This transition reshapes GLuc's surface cavities, which house residues critical for bioluminescence, including Phe72, Ile73 and Arg76 in pocket #1 and Trp142, Leu144, Arg147, and Phe151 in pocket #2. The interplay between these pockets in its structural transition between states is consistent with GLuc's reported positive cooperativity in coelenterazine substrate binding, characterized by a Hill coefficient of ~1.8[59,60]. Substrate binding at one pocket may enhance affinity at the other, facilitated by the structural changes observed during the closed-to-open transition. Additionally, the C-terminal helices H10 and H11 exhibit dynamic behavior, alternating between an ordered "broken helix" (in state 2) and a less ordered conformation (state 1), as indicated by pLDDT profiles (**Supplementary Figure S6**). These dynamic transitions are consistent with intermediate exchange broadening observed in ^{15}N relaxation data[28,31]. Together, these findings highlight how conformational changes in GLuc shape its functional binding pockets and regulate its bioluminescence activity.

Dynamic Structural Features of CDK2AP1. AF-NMR reveals two distinct conformational states of CDK2AP1 in dynamic equilibrium. In state 1 inter-chain sulfur– π interactions between Cys105 and Tyr63 contribute to the interface between helices H2 and H2'. In contrast, in state 2 these interactions switch to intra-chain sulfur–π interactions, resulting in a more compact structure. Sulfur–π interactions, although weaker than traditional hydrogen bonds or π–π stacking, still significantly contribute to protein stability and are frequently observed in protein structures, predominantly with sulfur positioned above the aromatic ring face (Ringer, 2007) as observed here for CDK2AP1.

The dynamic equilibrium between states 1 and 2 is supported by $RMSF_{ENS}$ vs $RMSF_{RCI}$ comparisons and NOESY Double Recall analysis, which identified unique NOEs for each state. Doubled resonances for Thr109 and Glu110 HNs further validate multiple states, reflecting distinct aromatic ring current shifts. Slow exchange between these states indicates that the two conformations of CDKAP1 interconvert on a timescale longer than milliseconds and that NOEs for the many other degenerate resonances of these two structurally-similar conformational states are overlapped (**Supplementary Figure S13**).

Although the conventional NMR structure (PDB: 2kw6) is high quality and fits the NOESY data well[47] (**Supplementary Table S11**), it does not fully capture the distinct states identified by AF-NMR. Some NMR models have short *intra*-chain Sγ–Cζ distances (<4 Å), but none exhibit short *inter*-chain Sγ–Cζ distances (< 4 Å) or full Tyr63 π–π stacking. Rather, these structures are distorted by conformational pinning[53], an artifact of interpreting NOEs arising from multiple states to restrain a single model. As a result, *inter*-chain S–π interactions were absent, while *intra*-chain S–π interactions (state 2-like) were overlooked. Additionally, the dynamic transition of cryptic pocket #3 from a closed state (state 2) to an open state (state 1), along with the identification of pockets #1 and #2 (**Supplementary Figure S14**), was not resolved in the restraint-based NMR models. These findings underscore the advantage of AF-NMR in capturing conformational heterogeneity and cryptic pockets.

The dynamic remodeling of CDK2AP1's pockets in the transition from state 2 (closed) to state 1 (open) may be functionally relevant for CDK2 binding and other interactions. Although Cys105 is critical for CDK2 interactions[48], mutation of Cys105 to Ala does not significantly disrupt CDK2AP1's dimeric structure [47]. Ablation of Cys105 - Tyr63 interactions is, however, expected to affect the dynamic equilibrium between states 1 and 2. Additionally, residues Thr109, Glu110, and Arg111 in pocket #1, which expands in the open state, has been proposed as a key CDK2 binding site in HEK-293 cells[39]. Beyond CDK2 binding, the positively charged residues in pockets #2 and #3 may facilitate interactions with other reported binding partners, such as negatively charged regions at the C-terminus of CHD3 and CHD4 in the NuRD complex[44,45]. Since pocket #3 is only present in state 1 (**Supplementary Figure S14)**, a transition from a closed to an open state may regulate accessibility to these interaction sites. These findings suggest that state-dependent pocket formation could modulate CDK2AP1's binding properties, influencing both CDK2 regulation and interactions with other partners.

Conclusions

In this study, we applied AFsample[21,50,61], an enhanced conformational sampling method originally developed for improving model predictions of protein complexes to generate diverse conformational states of GLuc and CDK2AP1. Using a Bayesian selection metric, models were selected based on their agreement with global NMR NOESY (*recall* score) and residue-specific chemical shift RCI data. Where AF-NMR revealed alternative conformational states, these were rigorously cross-validated using atom-

pair-specific NOESY data with Double Recall analysis. Our findings underscore the utility of modern AI-driven deep learning methods in generating realistic conformational states, including accurate models that can be identified and validated using experimental data. *Enhanced sampling methods proved invaluable in capturing structural heterogeneity and identifying regions of flexibility and rigidity that align with experimental RCI, NOE, and nuclear relaxation data*.

Beyond the systems studied here, AF-NMR has the potential to be broadly applied to investigate conformational heterogeneity and dynamics in a wide range of proteins, including proteins and complexes undergoing both large- and small-scale structural transitions. Multiple conformational states that can be more accurately captured by AF-NMR with enhanced sampling are particularly evident in regions of proteins where standard AF2 pLDDT values are high (i.e. high single-state model confidence), yet experimental chemical shift or nuclear relaxation data reveal underlying conformational variability. This is commonly observed in NMR studies of small proteins. By combining AI-based sampling and NMR-guided conformer selection, AF-NMR offers a powerful tool for studying protein dynamics and uncovering structural heterogeneity that cannot be resolved using conventional methods. These AF-NMR models provide a detailed framework for understanding these "hidden" states and their functional implications. The incorporation of additional experimental data types, such as residual dipolar couplings (RDCs), paramagnetic relaxation enhancements (PREs), or pseudocontact shifts (PCSs) and/or integration of emerging AI-based modeling methods, such as AlphaFold 3 or OpenFold, and advanced sampling techniques will further expand AF-NMR's applicability to more challenging systems, including large multimeric complexes and transiently populated states. These studies demonstrate how enhanced sampling combined with NMR data can uncover previously unrecognized structural and dynamic features, including cryptic pockets and alternative conformations, offering a powerful and evolving tool for studying protein dynamics, molecular recognition, and function.

Methods

Experimental NMR data. The published NMR structure of GLuc (PDB ID 7d2o) was determined using extensive ^{1}H,^{13}C and ^{15}N NMR assignments, along with ~2500 NOE-based distance restraints, including ~580 long-range restraints[28]. Chemical shift assignments were obtained from the BioMagResDatabase (BMRB ID 36385). NOESY peak lists and HetNOE data were provided by Wu, Kobayoshi, Kuroda, Yamazaki, and colleagues, who originally determined the NMR structure used for CASP14 structure prediction assessments[28,29], and are archived at https://zenodo.org/records/13831427.

The solution NMR structure of CDK2AP1 (PDB_ID 2kw6) was determined previously using standard triple-resonance NMR and 3D NOESY data, including 3D X-filtered NOESY data on a mixed sample of 50% [^{15}N, ^{13}C]-labeled and 50% unlabeled CDK2AP1 to resolve key inter-chain dimer NOEs[47]. NOESY peak lists and updated chemical shifts from BMRB ID 16808 (including newly assigned H58 - K62 resonances) were used for RPF analysis and AF-NMR model selection. To generate simulated NOESY peaks for AF-NMR states 1 and 2, we used *simulateNOE.pl*, a program developed for NMR-assisted CASP13 assessments[62]. The simulated peak lists were analyzed using Double Recall; peaks unique to each conformer were identified and used to guide further peak picking of weaker peaks at lower contours. An additional 124 NOESY peaks were picked by this iterative NOESY peak list refinement and used in the final Double Recall analysis [**Supplementary Table S7;** refined NOESY peak list available at (https://github.rpi.edu/RPIBioinformatics/AlphaFold-NMR)].

AlphaFold2 modeling. AF2 models were generated using the *ColabFold* server of AF-multimer (version 1.5.3) using default setups with no templates[63]. GLuc's ColabFold models were nearly identical to DeepMind's CASP14 AF2 models[29]. No X-ray crystal structures of GLuc or CDK2AP1 homologs were available in the PDB at the time of training AF2. The top five-ranked relaxed AF2 conformers included hydrogen atoms and per-residue pLDDT scores, as generated by the ColabFold pipeline.

AF2 enhanced sampling with AFsample. Enhanced sampling with AFsample was conducted as described by Wallner[21,50,61] using a modified *AlphaFold v2.2.0* pipeline[64] (https://github.com/bjornwallner/alphafoldv2.2.0), installed on the AiMOSx NPL cluster in the Center for Computational Innovation at Rensselaer Polytechnic Institute. The AF2 training set (PDB database from April 30, 2018) excluded NMR structures[1]. AFsample calculations, which use six different distinct dropout settings[21,50,61] to generate ~6000 diverse structural models. Hydrogen atoms were added using *run_relax_from_results_pkl.py* from the AFsample package. AFsample is quite aggressive in generating conformational diversity, and computes some models that are not physically reasonable, with incorrect amino acid chirality, non-native cis peptide bonds, missing residues, and other biophysically incorrect features, particularly in the not-well-packed residue segments. The most egregious of these physically unreasonable models were identified and removed, as described elsewhere (Spaman et al, manuscript in preparation). Final datasets included 4,990 relaxed models for GLuc and 5984 relaxed models for CDK2AP1. The pTM scores were retrieved from AF2 output files (*result_model_*.pkl.json*), and pLDDT scores from atomic coordinate files.

Knowledge-based protein structure validation. All model quality assessments were performed using the *Protein Structure Validation Software* (*PSVS* v2.0)[65] (https://montelionelab.chem.rpi.edu/PSVS/PSVS2/) and the protein model assessment program *PDBStat* (Tejero *et al*., 2013). *PSVS* runs a suite of knowledge-based software tools including *ProCheck* (v3.5.4) (Laskowski *et al*., 1993) and *MolProbity* (v6.35.040409)[66]. Validation scores were normalized as Z-scores, referenced against mean values obtained for 252 high-resolution (<1.8 Å) X-ray structures. For all metrics assessed, positive Z scores indicate 'better' scores[65].

NMR NOESY RPF-DP scores. RPF-DP scores provide a rapid and sensitive assessment of how well a structural model agrees with 3D ^{15}N and ^{13}C-resolved NOESY peak lists and resonance assignments, serving as a measure of structure accuracy[29,67,68]. These scores were computed using the *RPF server* (ASDP ver 1.0) https://montelionelab.chem.rpi.edu/rpf/. *RPF* scoring includes several key metrics: *recall*, the fraction of NOESY peaks explained by the model (or collection of models); *precision*, the fraction of short interproton distances in the model(s) supported by NOESY peaks; *F-measure*, the geometric mean of recall and precision; and *discriminating power* (*DP)*, a normalized F-measure that accounts for NOESY data completeness and the expected baseline for a random coil structure[29,67,68]. RPF-DP scores serve as an NMR equivalent to an "R-factor", allowing model evaluation against unassigned NOESY peak list data. Output folders (zip files) were downloaded from the *RPF server* for further Double Recall analysis (described below).

NMR NOESY Double Recall analysis. Double Recall analysis (v1.0) was performed in a Jupyter notebook to compare two conformer ensembles (A vs B) and identify NOEs uniquely explained by each. The method uses *RPF* recall violation reports from zipped RPF output files to determine NOEs that correspond to short inter-proton distances present in only one ensemble. NOEs unique to ensemble A are plotted in blue, while those unique to ensemble B are in orange. The results are displayed in a contact

map-like 2D plot, where the x-axis represents the residue number of the first H(-N/C) proton ("1H(-N/C)-donor Match") and the y-axis represents the residue number of the second proton ("1H-acceptor Match"). Multiple NOEs between the same residue pairs appear as a single dot. A 1D histogram at the top of the plot shows the per-residue count of uniquely matched NOEs along the x-axis, which have higher-confidence assignments due to the additional frequency resolution provided by the attached ^{15}N or ^{13}C nucleus.

Double Recall analysis allows for comparison of any two conformer ensembles by evaluating their midrange interproton distances for the NOESY peak comparison. The method was further extended to compare combined multi-state ensembles against a reference ensemble by using the shortest midrange interproton distances across merged conformational states. In either case, the number of models in each conformer ensemble does not need to be identical for a valid comparison.

Well-defined residue ranges and TM scores to reference structures. Well-defined residue ranges for NMR and AF2 ensembles were determined using Cyrange[69] and applied to structural superimpositions, quality assessments, and TM score calculations[70]. For TM-score comparisons, the medoid conformer[71] of the NMR_{7d2o} ensemble was used, with the corresponding well-defined residues. Similarly, AF2 TM-scores were calculated using the rank1 conformer, restricted to its well-defined residues.

Per-residue Random Coil Index (RCI) and $RMSF_{RCI}$. RCI values were computed using the Wishart server[72] (http://www.randomcoilindex.ca/cgi-bin/rci_cgi_current.py), applying default options:

$$RCI = (\langle A|\Delta\delta C\alpha| + B|\Delta\delta CO| + C|\Delta\delta C\beta| + D|\Delta\delta N| + E|\Delta\delta NH| + F|\Delta\delta H\alpha|\rangle)^{-1} \qquad \text{Eqn. 1}$$

where $|\Delta\delta C\alpha|$, $|\Delta\delta CO|$, $|\Delta\delta C\beta|$, $|\Delta\delta N|$, $|\Delta\delta NH|$ and $|\Delta\delta H\alpha|$ are the absolute values of the conformation-dependent chemical shifts $\Delta\delta X = \delta X_{observed} - \delta X_{random_coil}$ (in ppm) of Cα, CO, Cβ, N, NH and Hα resonance, respectively, and *A*, *B*, *C*, *D*, *E* and *F* are weighting coefficients. Left angle and right angle brackets (<·>) indicate that the RCI per residue is the average value across the several resonances (^{1}H, ^{13}C, and ^{15}N) of that residue. If any per-residue RCI value exceeds 0.6, it is replaced with the ceiling limit of 0.6. After this, a second smoothing along the sequence of RCI values is done using three-point averaging to obtain the final RCI values as previously described[72].

Root-mean-square-fluctuations based on RCIs ($RMSF_{RCI}$), were calculated as previously described[72]:

$$RMSF_{RCI} = RCI * 12.7 \text{ Å} \qquad \text{Eqn. 2}$$

Comparison SEM plots: pLDDT vs RCI and $RMSF_{ENS}$ vs $RMSF_{RCI}$. RCI values were scaled to the 0.0-1.0 range ($RCI_{0.6} = RCI/0.6$) for comparison with pLDDT scores. For pLDDT vs RCI plots, per-model per-residue pLDDT, ensemble-average per-residue pLDDT ($pLDDT_{avg}$) and $RCI_{0.6}$ values were plotted along the sequence to assess correlation. In most cases we have examined, RCI and pLDDT (or $pLDDT_{avg}$) have an inverse correlation. The comparison plots were constructed by summing $RCI_{0.6}$ and $pLDDT_{avg}$ values per residue, with global mean and standard deviation (SD) calculated. Confidence intervals (95% CI) were determined using the CI t-test with one degree of freedom:

$$CI_p = SEM \cdot Z_p \qquad \text{Eqn. 3}$$

where the standard error of the mean, SEM = SD / $(N-1)^{½}$. N is the number of residues with pLDDT > 50 and available RCI values, and Z_p=12.71 (p=95%). Mean and CI values are displayed as dashed lines highlighting significant deviations. Residues with pLDDT ≤ 50 were excluded from the mean, SD, and CI calculations.

Similarly, for $RMSF_{ENS}$ vs $RMSF_{RCI}$ comparison SEM plots, atomic coordinate ensemble RMSF ($RMSF_{ENS}$) values and $RMSF_{RCI}$ (Eqn. 2) values were plotted along the sequence, with differences between $RMSF_{RCI}$ and $RMSF_{ENS}$ reported per residue. $RMSF_{ENS}$ was computed using Bio3D[74] in R.

Statistical Correlation Coefficients. Spearman Correlation Coefficient (SCC) and Lin's Concordance Correlation Coefficient (CCC) were calculated with R as described elsewhere[73]. The CCC is the concordance between a new test or measurement (e.g. $RMSF_{ENS}$) and a standard test or measurement (e.g. $RMSF_{RCI}$). It obeys the inequality $-1 \leq -|PCC| \leq CCC \leq +|PCC| \leq +1$, where PCC is Pearson's correlation coefficient.

Principal Component, Clustering, and RMSF analysis. To examine structural diversity across various models, principal component analysis (PCA) was conducted using Bio3D[74]. PCA was applied to Cα-Cα distance matrices to capture the primary structural variations among the models. Agglomerative hierarchical clustering[75] was employed to group similar conformers into well-separated distinct clusters (states) based on PC1, PC2, and PC3.

Bayesian model selection metric using NOE and RCI data. To quantify agreement between computational models and experimental data, an AF-NMR Bayesian model selection metric was developed, incorporating both NOE recall and RCI correlation scores. This approach estimates the likelihood of a model given NOE and RCI data using Bayes' theorem.

To estimate how well the model fits the NOE data, the Bayesian **P(model | NOE) score** uses the scaled NOESY recall scores:

$$P(NOE \mid model) = (recall(model) - recall_min) / (recall_max - recall_min) \qquad \text{Eqn. 4}$$

where recall_max and recall_min are the highest and lowest NOESY recall scores across all models.

The overall model probability, P(model), is estimated using the AF2 pTM metric[1], a measure of overall structural confidence/reliability. We decided to use the pTM, rather than <pLDDT> (the average pLDDT value along the sequence) since both pTM and NOESY recall are global rather than per-residues scores. The Bayesian probability of a model given NOE data is then:

$$P(model \mid NOE) \sim P(NOE \mid model) * P(model) \sim P(NOE \mid model) * pTM \qquad \text{Eqn. 5}$$

For scoring models, we use:

$$P(model \mid NOE) = [P(NOE \mid model) * pTM]^{1/2} \qquad \text{Eqn. 6}$$

This metric incorporates both the agreement of the model with NOE data and the model's reliability as estimated by pTM.

Similarly, to estimate P(model | RCI) for each model, we calculate the SCC between per-residue pLDDT scores and RCI (chemical shift) values:

$$P(RCI \mid model) \sim |SCC(pLDDT, RCI)| \qquad \text{Eqn. 7}$$

This score evaluates the agreement between pLDDT, a per-residue reliability estimate from AF2 structure models, and the per-residue NMR RCI values derived from chemical shift data, an experimental estimate of conformational flexibility. Un-normalized Bayesian likelihood is then estimated as:

$$P(model \mid RCI) \sim P(RCI \mid model) * P(model) \sim |SCC(pLDDT, RCI)| * \langle pLDDT \rangle \qquad \text{Eqn. 8}$$

where both |SCC(pLDDT, RCI)| and <pLDDT> are scaled between 0.0 and 1.0. We used SCC instead of PCC due to the observed nonlinear relationship between pLDDT and RCI, and because SCC is less influenced by disordered tails. Vranken and co-workers report PCC(pLDDT, S^2_{RCI}) = 0.673 for a database of 76,711 residues[13], supporting its use as a binary indicator of order vs disorder, although the AF2 pLDDT metric does not linearly correlate with the degree of dynamics within highly disordered regions of proteins. Previous studies have also shown that RCI correlates with local rigidity inferred from NMR structures based on hydrogen bond network satisfaction[76], a correlation that was used as an estimate of NMR model accuracy.

For the purpose of scoring models vs RCI data, we use:

$$P(model \mid RCI) = [|SCC(pLDDT, RCI)| * \langle pLDDT \rangle]^{1/2} \qquad \text{Eqn. 9}$$

Each model is given an **AF-NMR selection score** using the Bayesian estimate of model likelihood given both RCI and NOE:

$$P(model \mid NOE, RCI) = (P(model \mid NOE) + P(model \mid RCI)) / 2 \qquad \text{Eqn. 10}$$

In this study, we define the **AF-NMR Bayesian model selection metric** as:

$$P(model \mid NMR\ data) \equiv P(model \mid NOE, RCI) \qquad \text{Eqn. 11}$$

This metric enables quantitative selection of models that best match experimental data, and can also be extended to incorporate additional experimental data, such as RDCs.

Conformational selection and state combination assessment for multi-state modeling. To identify conformer ensembles that best fit experimental data, models generated by enhanced sampling are grouped using PCA-based hierarchical clustering and scored with the AF-NMR Bayesian model selection metric. The top five models from each cluster are selected as candidate single-state ensembles. These ensembles are ranked from high to low by their average Bayesian Model Selection scores, and labeled sequentially with Greek letters (e.g., ensembles α5, β5, γ5 and clusters α, β, γ, where 5 refers to the number of conformers in the corresponding ensemble). The highest-scoring five-conformer ensemble, α5, is assigned as state 1.

To evaluate whether a multi-state ensemble better explains the data, we iteratively test combinations of the potential states. The RMSF agreement between the atomic coordinates of state 1 ($RMSF_{ENS}$) and the RMSF estimated from RCI data ($RMSF_{RCI}$) is first evaluated as:

$$CCC_{state1} = CCC(RMSF_{ENS}(\text{state } 1), RMSF_{RCI}) \quad \text{if } CCC(RMSF_{ENS}(\text{state } 1), RMSF_{RCI}) > 0; \quad \text{otherwise, } CCC_{state1} = 0 \text{ and exit} \qquad \text{Eqn. 12a}$$

where the CCC function measures the agreement between the model-derived Cα $RMSF_{ENS}$ and $RMSF_{RCI}$. Next, we assess whether adding a second candidate single-state ensemble *x* improves the correlation:

$$CCC_{state1+x} = CCC(RMSF_{ENS}(\text{state } 1 + x), RMSF_{RCI}) \quad \text{if } CCC(RMSF_{ENS}(\text{state } 1 + x), RMSF_{RCI}) > CCC_{state1}; \quad \text{otherwise, } CCC_{state1+x} = 0 \text{ and ensemble } x \text{ is eliminated from further state combinations} \qquad \text{Eqn. 12b}$$

Only ensembles that improve these CCCs are retained, and the ensemble that gives the highest combined CCC becomes state 2. The process of adding and testing new ensembles is repeated until no additional states improve the fit to experimental data.

A comparison plot of $RMSF_{ENS}$ of the final assigned state(s) vs $RMSF_{RCI}$ is evaluated. If most differences fall within the 95% CI, then these state(s) define the solution NMR structure. If at least two distinct states are identified, the result is a multi-state structure. Models with large deviations beyond the 95% CI and a final combined CCC < 0.4 suggest an inaccurate structural representation, requiring alternative modeling strategies to generate more diverse conformers.

Molecular graphics*, *secondary structure analysis, and pocket analysis. Structural visualization and molecular graphics were done using *ChimeraX*[77] and *PyMol*[78]. The *Define Secondary Structure of Proteins (DSSP)*[79] server (https://2struc.cryst.bbk.ac.uk/twostruc) was used for identifying regular secondary structures. The *CastpFold* server[52] was used for surface pocket analysis.

Acknowledgments
We thank T. Benavides, N. Dube, A. Ertekin, K. Fraga, Y. Kuroda, E. Li, B. A. Shurina, G.V.T. Swapna, R. Tejero, and N. Wu for helpful discussions, and S. Collen for his efforts in installing and maintaining AFsample on the NPL CPU / GPU cluster of the RPI Center for Computational Innovations. This research was supported by grant R35-GM141818 (to GTM) from the National Institutes of Health, National Institute of General Medical Sciences.

Author Contributions
YJH, TAR, LES, and GTM conceptualized the study and analyzed data. TAR, LES, and NK provided experimental data. NK provided expertise with GLuc NMR data. YJH developed computer codes. All authors contributed in writing and editing the manuscript.

Data Availability
Atomic models of GLuc State 1 and State 2 (PDB_ID 9A8V, linked to data including NOESY peak lists and chemical shifts at https://zenodo.org/records/13831427) and CDK2AP1 State1 and State 2 (PDB_ID 9A8Z, linked to data including NOESY peak lists and chemical shifts at BMRB 16808) have been deposited in the Protein Data Bank. Additional data such as AFsample models and their scores are available at GitHub (https://github.rpi.edu/RPIBioinformatics/AlphaFold-NMR)

Code Availability
Scripts for AF-NMR analysis presented here are available at GitHub (https://github.rpi.edu/RPIBioinformatics/AlphaFold-NMR)

Declaration of Interests
GTM is a founder of Nexomics Biosciences, Inc. This does not represent a conflict of interest for this study.

References

1 Jumper, J. *et al.* Highly accurate protein structure prediction with AlphaFold. *Nature* **596**, 583-589 (2021). https://doi.org:10.1038/s41586-021-03819-2
2 Terwilliger, T. C. *et al.* AlphaFold predictions are valuable hypotheses and accelerate but do not replace experimental structure determination. *Nat Methods* **21**, 110-116 (2024). https://doi.org:10.1038/s41592-023-02087-4
3 Terwilliger, T. C. *et al.* Improved AlphaFold modeling with implicit experimental information. *Nat Methods* **19**, 1376-1382 (2022). https://doi.org:10.1038/s41592-022-01645-6
4 Robertson, A. J., Courtney, J. M., Shen, Y., Ying, J. & Bax, A. Concordance of X-ray and AlphaFold2 models of SARS-CoV-2 main protease with residual dipolar couplings measured in solution. *J Am Chem Soc* **143**, 19306-19310 (2021). https://doi.org:10.1021/jacs.1c10588
5 Fontana, P. *et al.* Structure of cytoplasmic ring of nuclear pore complex by integrative cryo-EM and AlphaFold. *Science* **376**, eabm9326 (2022).
6 Tejero, R., Huang, Y. J., Ramelot, T. A. & Montelione, G. T. AlphaFold Models of small proteins rival the accuracy of solution NMR structures. *Front Mol Biosci* **9**, 877000 (2022). https://doi.org:10.3389/fmolb.2022.877000
7 Li, E. H. *et al.* Blind assessment of monomeric AlphaFold2 protein structure models with experimental NMR data. *J Magn Reson* **352**, 107481 (2023). https://doi.org:10.1016/j.jmr.2023.107481
8 Chinnam, N. B. *et al.* Combining small angle X-ray scattering (SAXS) with protein structure predictions to characterize conformations in solution. *Methods Enzymol* **678**, 351-376 (2023). https://doi.org:10.1016/bs.mie.2022.09.023
9 Ruff, K. M. & Pappu, R. V. AlphaFold and implications for intrinsically disordered proteins. *J Mol Biol* **433**, 167208 (2021). https://doi.org:10.1016/j.jmb.2021.167208
10 Guo, H. B. *et al.* AlphaFold2 models indicate that protein sequence determines both structure and dynamics. *Sci Rep* **12**, 10696 (2022). https://doi.org:10.1038/s41598-022-14382-9
11 Saldano, T. *et al.* Impact of protein conformational diversity on AlphaFold predictions. *Bioinformatics* **38**, 2742-2748 (2022). https://doi.org:10.1093/bioinformatics/btac202

12 Ma, P., Li, D. W. & Bruschweiler, R. Predicting protein flexibility with AlphaFold. *Proteins* **91**, 847-855 (2023). https://doi.org:10.1002/prot.26471
13 Gavalda-Garcia, J., Dixit, B., Diaz, A., Ghysels, A. & Vranken, W. Gradations in protein dynamics captured by experimental NMR are not well represented by AlphaFold2 models and other computational metrics. *J Mol Biol* **437**, 168900 (2025). https://doi.org:10.1016/j.jmb.2024.168900
14 Del Alamo, D., Sala, D., McHaourab, H. S. & Meiler, J. Sampling alternative conformational states of transporters and receptors with AlphaFold2. *Elife* **11** (2022). https://doi.org:10.7554/eLife.75751
15 Heo, L. & Feig, M. Multi-state modeling of G-protein coupled receptors at experimental accuracy. *Proteins* **90**, 1873-1885 (2022). https://doi.org:10.1002/prot.26382
16 Stein, R. A. & McHaourab, H. S. SPEACH_AF: Sampling protein ensembles and conformational heterogeneity with Alphafold2. *PLOS Computational Biology* **18**, e1010483 (2022). https://doi.org:10.1371/journal.pcbi.1010483
17 Sala, D., Engelberger, F., McHaourab, H. S. & Meiler, J. Modeling conformational states of proteins with AlphaFold. *Curr Opin Struct Biol* **81**, 102645 (2023). https://doi.org:10.1016/j.sbi.2023.102645
18 Sala, D., Hildebrand, P. W. & Meiler, J. Biasing AlphaFold2 to predict GPCRs and kinases with user-defined functional or structural properties. *Front Mol Biosci* **10**, 1121962 (2023). https://doi.org:10.3389/fmolb.2023.1121962
19 Jing, B., Berger, B. & Jaakkola, T. AlphaFold meets flow matching for generating protein ensembles. *arXiv:2402.04845* (2024).
20 Wayment-Steele, H. K. *et al.* Predicting multiple conformations via sequence clustering and AlphaFold2. *Nature* **625**, 832-839 (2024). https://doi.org:10.1038/s41586-023-06832-9
21 Wallner, B. AFsample: improving multimer prediction with AlphaFold using massive sampling. *Bioinformatics* **39** (2023). https://doi.org:10.1093/bioinformatics/btad573
22 Kalakoti, Y. & Wallner, B. AFsample2: Predicting multiple conformations and ensembles with AlphaFold2. *bioRxiv*, 2024.2005.2028.596195 (2024). https://doi.org:10.1101/2024.05.28.596195
23 Sedinkin, S. L., Burns, D., Shukla, D., Potoyan, D. A. & Venditti, V. Solution structure ensembles of the open and closed forms of the approximately 130 kDa enzyme I via AlphaFold modeling, coarse grained simulations, and NMR. *J Am Chem Soc* **145**, 13347-13356 (2023). https://doi.org:10.1021/jacs.3c03425
24 Monteiro da Silva, G., Cui, J. Y., Dalgarno, D. C., Lisi, G. P. & Rubenstein, B. M. High-throughput prediction of protein conformational distributions with subsampled AlphaFold2. *Nat Commun* **15**, 2464 (2024). https://doi.org:10.1038/s41467-024-46715-9
25 Zheng, S. *et al.* Predicting equilibrium distributions for molecular systems with deep learning. *Nature Machine Intelligence* (2024). https://doi.org:10.1038/s42256-024-00837-3
26 Tejero, R., Snyder, D., Mao, B., Aramini, J. M. & Montelione, G. T. PDBStat: a universal restraint converter and restraint analysis software package for protein NMR. *J Biomol NMR* **56**, 337-351 (2013). https://doi.org:10.1007/s10858-013-9753-7
27 Baskaran, K. *et al.* Restraint validation of biomolecular structures determined by NMR in the Protein Data Bank. *Structure* (2024). https://doi.org:10.1016/j.str.2024.02.011
28 Wu, N. *et al.* Solution structure of *Gaussia* Luciferase with five disulfide bonds and identification of a putative coelenterazine binding cavity by heteronuclear NMR. *Sci Rep* **10**, 20069 (2020). https://doi.org:10.1038/s41598-020-76486-4

29 Huang, Y. J. *et al.* Assessment of prediction methods for protein structures determined by NMR in CASP14: Impact of AlphaFold2. *Proteins* **89**, 1959-1976 (2021). https://doi.org:10.1002/prot.26246
30 Kaskova, Z. M., Tsarkova, A. S. & Yampolsky, I. V. 1001 lights: luciferins, luciferases, their mechanisms of action and applications in chemical analysis, biology and medicine. *Chem Soc Rev* **45**, 6048-6077 (2016). https://doi.org:10.1039/c6cs00296j
31 Wu, N., Kobayashi, N., Kuroda, Y. & Yamazaki, T. Reflecting on mutational and biophysical analysis of *Gaussia* princeps Luciferase from a structural perspective: a unique bioluminescent enzyme. *Biophys Rev* **14**, 1513-1520 (2022). https://doi.org:10.1007/s12551-022-01025-6
32 Dijkema, F. M. *et al.* A suicidal and extensively disordered luciferase with a bright luminescence. *Protein Sci* **33**, e5115 (2024). https://doi.org:10.1002/pro.5115
33 Zweckstetter, M. NMR hawk-eyed view of AlphaFold2 structures. *Protein Sci* **30**, 2333-2337 (2021). https://doi.org:10.1002/pro.4175
34 McDonald, E. F., Jones, T., Plate, L., Meiler, J. & Gulsevin, A. Benchmarking AlphaFold2 on peptide structure prediction. *Structure* **31**, 111-119 e112 (2023). https://doi.org:10.1016/j.str.2022.11.012
35 Bonin, J. P., Aramini, J. M., Dong, Y., Wu, H. & Kay, L. E. AlphaFold2 as a replacement for solution NMR structure determination of small proteins: Not so fast! *J. Magn. Reson.* (2024). https://doi.org:10.1016/j.jmr.2024.107725
36 Bryant, P. & Noe, F. Structure prediction of alternative protein conformations. *Nat Commun* **15**, 7328 (2024). https://doi.org:10.1038/s41467-024-51507-2
37 Chakravarty, D. *et al.* AlphaFold predictions of fold-switched conformations are driven by structure memorization. *Nat Commun* **15**, 7296 (2024). https://doi.org:10.1038/s41467-024-51801-z
38 Lazou, M. *et al.* Predicting multiple conformations of ligand binding sites in proteins suggests that AlphaFold2 may remember too much. *Proc Natl Acad Sci U S A* **121**, e2412719121 (2024). https://doi.org:10.1073/pnas.2412719121
39 Shintani, S. *et al.* p12DOC-1 Is a Novel Cyclin-Dependent Kinase 2-Associated Protein. *Molecular and Cellular Biology* **20**, 6300-6307 (2000). https://doi.org:10.1128/MCB.20.17.6300-6307.2000
40 He, X. *et al.* CDK2-AP1 inhibits growth of breast cancer cells by regulating cell cycle and increasing docetaxel sensitivity in vivo and in vitro. *Cancer Cell Int* **14**, 130 (2014). https://doi.org:10.1186/s12935-014-0130-8
41 Gera, R., Mokbel, L., Jiang, W. G. & Mokbel, K. mRNA Expression of CDK2AP1 in Human Breast Cancer: Correlation with Clinical and Pathological Parameters. *Cancer Genomics Proteomics* **15**, 447-452 (2018). https://doi.org:10.21873/cgp.20103
42 Che, Y., Wang, G. & Xia, Q. CDK2AP1 influences immune infiltrates and serves as a prognostic indicator for hepatocellular carcinoma. *Front Genet* **13**, 937310 (2022). https://doi.org:10.3389/fgene.2022.937310
43 Wong, D. T., Kim, J. J., Khalid, O., Sun, H. H. & Kim, Y. Double edge: CDK2AP1 in cell-cycle regulation and epigenetic regulation. *J Dent Res* **91**, 235-241 (2012). https://doi.org:10.1177/0022034511420723
44 Spruijt, C. G. *et al.* CDK2AP1/DOC-1 is a bona fide subunit of the Mi-2/NuRD complex. *Mol Biosyst* **6**, 1700-1706 (2010). https://doi.org:10.1039/c004108d

45 Spruijt, C. G., Grawe, C., Kleinendorst, S. C., Baltissen, M. P. A. & Vermeulen, M. Cross-linking mass spectrometry reveals the structural topology of peripheral NuRD subunits relative to the core complex. *FEBS J* **288**, 3231-3245 (2021). https://doi.org:10.1111/febs.15650
46 Torchy, M. P., Hamiche, A. & Klaholz, B. P. Structure and function insights into the NuRD chromatin remodeling complex. *Cell Mol Life Sci* **72**, 2491-2507 (2015). https://doi.org:10.1007/s00018-015-1880-8
47 Ertekin, A. *et al.* Human Cyclin-dependent Kinase 2-associated Protein 1 (CDK2AP1) Is Dimeric in Its Disulfide-reduced State, with Natively Disordered N-terminal Region. *Journal of Biological Chemistry* **287**, 16541-16549 (2012). https://doi.org:10.1074/jbc.M112.343863
48 Kim, Y., Ohyama, H., Patel, V., Figueiredo, M. & Wong, D. T. Mutation of Cys¹⁰⁵ Inhibits Dimerization of p12$^{CDK2-AP1}$ and Its Growth Suppressor Effect *. *Journal of Biological Chemistry* **280**, 23273-23279 (2005). https://doi.org:10.1074/jbc.M412929200
49 Piovesan, D., Monzon, A. M. & Tosatto, S. C. E. Intrinsic protein disorder and conditional folding in AlphaFoldDB. *Protein Science* **31**, e4466 (2022). https://doi.org:https://doi.org/10.1002/pro.4466
50 Wallner, B. Improved multimer prediction using massive sampling with AlphaFold in CASP15. *Proteins* **91**, 1734-1746 (2023). https://doi.org:10.1002/prot.26562
51 Wu, N. *et al.* A Structural Model of Truncated *Gaussia* princeps Luciferase Elucidating the Crucial Catalytic Function of No.76 Arginine towards Coelenterazine Oxidation. *PLoS Comput Biol* **21**, e1012722 (2025). https://doi.org:10.1371/journal.pcbi.1012722
52 Ye, B., Tian, W., Wang, B. & Liang, J. CASTpFold: Computed Atlas of Surface Topography of the universe of protein Folds. *Nucleic Acids Res* **52**, W194-W199 (2024). https://doi.org:10.1093/nar/gkae415
53 Tejero, R., Bassolino-Klimas, D., Bruccoleri, R. E. & Montelione, G. T. Simulated annealing with restrained molecular dynamics using CONGEN: energy refinement of the NMR solution structures of epidermal and type-alpha transforming growth factors. *Protein Sci* **5**, 578-592 (1996). https://doi.org:10.1002/pro.5560050403
54 Lindorff-Larsen, K., Best, R. B., DePristo, M. A., Dobson, C. M. & Vendruscolo, M. Simultaneous determination of protein structure and dynamics. *Nature* **433**, 128-132 (2005). https://doi.org:10.1038/nature03199
55 Abramson, J. *et al.* Accurate structure prediction of biomolecular interactions with AlphaFold 3. *Nature* **630**, 493-500 (2024). https://doi.org:10.1038/s41586-024-07487-w
56 Baek, M. *et al.* Accurate prediction of protein structures and interactions using a three-track neural network. *Science* (2021). https://doi.org:10.1126/science.abj8754
57 Ahdritz, G. *et al.* OpenFold: retraining AlphaFold2 yields new insights into its learning mechanisms and capacity for generalization. *Nature Methods* (2024). https://doi.org:10.1038/s41592-024-02272-z
58 Lin, Z. *et al.* Evolutionary-scale prediction of atomic-level protein structure with a language model. *Science* **379**, 1123-1130 (2023). https://doi.org:10.1126/science.ade2574
59 Tzertzinis, G., Schildkraut, E. & Schildkraut, I. Substrate cooperativity in marine luciferases. *PLoS One* **7**, e40099 (2012). https://doi.org:10.1371/journal.pone.0040099
60 Larionova, M. D., Markova, S. V. & Vysotski, E. S. Bioluminescent and structural features of native folded *Gaussia* luciferase. *J Photochem Photobiol B* **183**, 309-317 (2018). https://doi.org:10.1016/j.jphotobiol.2018.04.050

61 Johansson-Akhe, I. & Wallner, B. Improving peptide-protein docking with AlphaFold-Multimer using forced sampling. *Front Bioinform* **2**, 959160 (2022). https://doi.org:10.3389/fbinf.2022.959160
62 Sala, D. *et al.* Protein structure prediction assisted with sparse NMR data in CASP13. *Proteins* **87**, 1315-1332 (2019). https://doi.org:10.1002/prot.25837
63 Mirdita, M. *et al.* ColabFold: making protein folding accessible to all. *Nat Methods* **19**, 679-682 (2022). https://doi.org:10.1038/s41592-022-01488-1
64 Evans, R. *et al.* Protein complex prediction with AlphaFold-Multimer. *bioRxiv*, 2021.2010.2004.463034 (2022). https://doi.org:10.1101/2021.10.04.463034
65 Bhattacharya, A., Tejero, R. & Montelione, G. T. Evaluating protein structures determined by structural genomics consortia. *Proteins* **66**, 778-795 (2007). https://doi.org:10.1002/prot.21165
66 Chen, V. B. *et al.* MolProbity: all-atom structure validation for macromolecular crystallography. *Acta crystallographica. Section D, Biological crystallography* **66**, 12-21 (2010). https://doi.org:10.1107/S0907444909042073
67 Huang, Y. J., Powers, R. & Montelione, G. T. Protein NMR recall, precision, and F-measure scores (RPF scores): structure quality assessment measures based on information retrieval statistics. *J Am Chem Soc* **127**, 1665-1674 (2005). https://doi.org:10.1021/ja047109h
68 Huang, Y. J., Rosato, A., Singh, G. & Montelione, G. T. RPF: a quality assessment tool for protein NMR structures. *Nucleic Acids Research* **40**, W542-546 (2012). https://doi.org:10.1093/nar/gks373
69 Kirchner, D. K. & Guntert, P. Objective identification of residue ranges for the superposition of protein structures. *BMC Bioinformatics* **12**, 170 (2011). https://doi.org:10.1186/1471-2105-12-170
70 Zhang, Y. & Skolnick, J. Scoring function for automated assessment of protein structure template quality. *Proteins: Structure, Function, and Bioinformatics* **57**, 702-710 (2004).
71 Montelione, G. T. *et al.* Recommendations of the wwPDB NMR Validation Task Force. *Structure* **21**, 1563-1570 (2013). https://doi.org:10.1016/j.str.2013.07.021
72 Berjanskii, M. V. & Wishart, D. S. The RCI server: rapid and accurate calculation of protein flexibility using chemical shifts. *Nucleic Acids Res* **35**, W531-537 (2007). https://doi.org:10.1093/nar/gkm328
73 Lin, L., Hedayat, A. S., Sinha, B. & Yang, M. Statistical methods in assessing agreement. *J Am Stat Assoc* **97**, 257 - 270 (2002). https://doi.org:10.1198/016214502753479392
74 Grant, B. J., Skjaerven, L. & Yao, X. Q. The Bio3D packages for structural bioinformatics. *Protein Sci* **30**, 20-30 (2021). https://doi.org:10.1002/pro.3923
75 Kaufman, L. & Rousseeuw, P. J. *Finding Groups in Data: An Introduction to Cluster Analysis.*, (Wiley).
76 Fowler, N. J., Sljoka, A. & Williamson, M. P. A method for validating the accuracy of NMR protein structures. *Nat Commun* **11**, 6321 (2020). https://doi.org:10.1038/s41467-020-20177-1
77 Meng, E. C. *et al.* UCSF ChimeraX: Tools for structure building and analysis. *Protein Sci* **32**, e4792 (2023). https://doi.org:10.1002/pro.4792
78 PyMOL (2020).
79 Kabsch, W. & Sander, C. Dictionary of protein secondary structure: pattern recognition of hydrogen-bonded and geometrical features. *Biopolymers* **22**, 2577-2637 (1983). https://doi.org:10.1002/bip.360221211